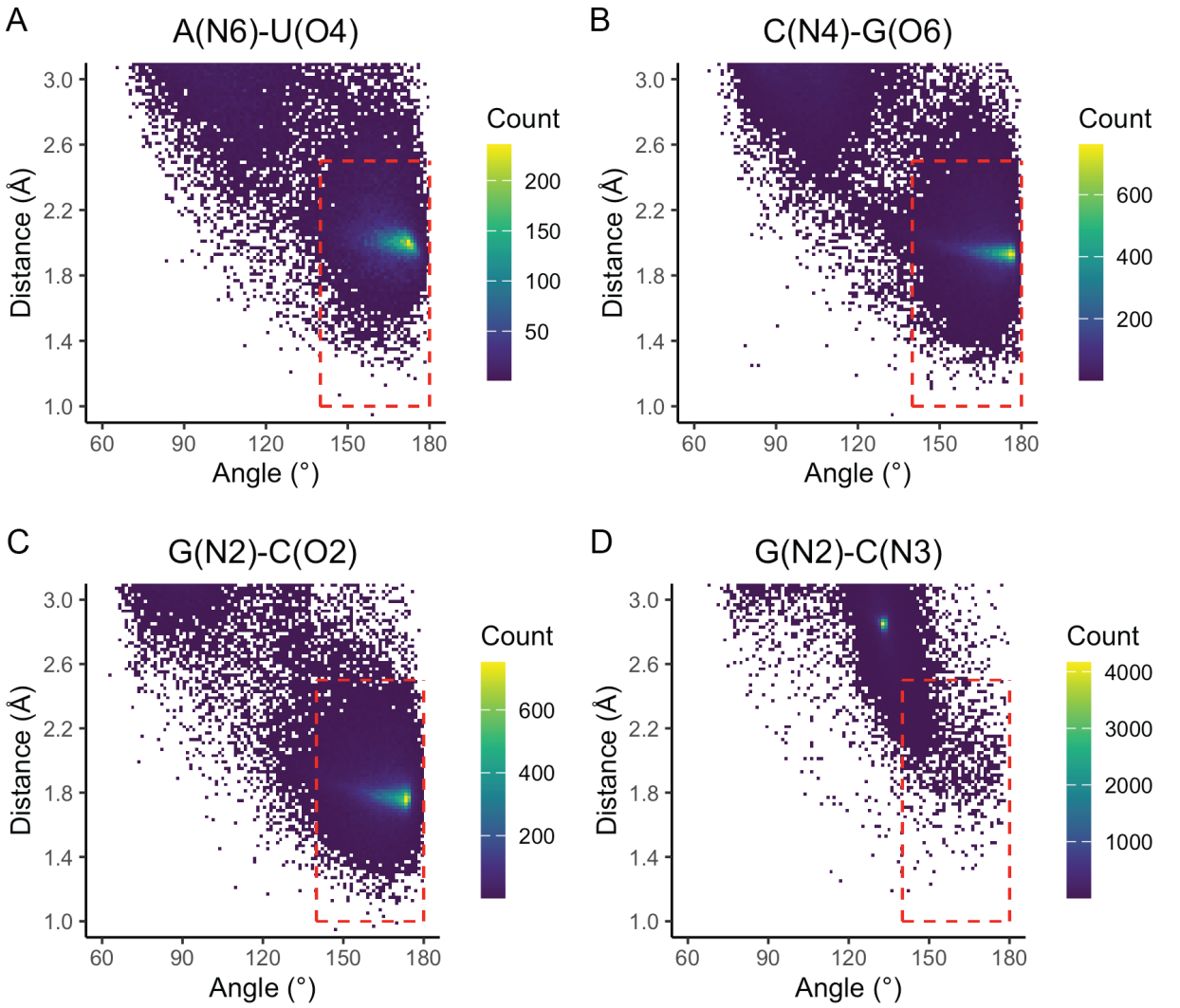

Figure S1. Amine-acceptor pair measurements for specific atom pairs in WCF pairs. (*A-D*) Heatmaps illustrating the amine-acceptor geometries of A(N6)-U(O4), C(N4)-G(O6), G(N2)-C(O2), and G(N2)-C(N3) pairs, respectfully. Any pairs with distance and angle measurements that fall within the dashed red box are considered H-bonding. The interactions in these four panels were excluded from Figure 3A.

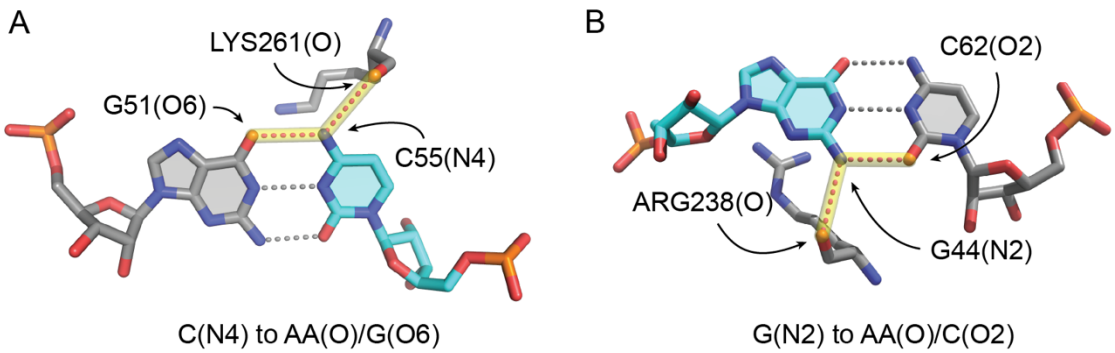

Figure S2. Examples of dual-donating amines involving amino acid backbone carbonyl acceptors. (*A*-*B*) C55 and G44 in (*A*) and (*B*), respectfully, form canonical GC base pairs and donate an additional H-bond via their amine to a nearby amino acid backbone carbonyl. C55 and G44 are both from chain E of PDB ID 7XJG (Wang et al. 2022). In both panels, magenta dots highlighted in yellow depict H-bonds from dual-donating amines. Grey dots represent other H-bonds. All instances of these dual-donor-to-acceptor-pair interactions are provided within CSV and Python files; see Supplemental Table S1 and Supplemental Materials.

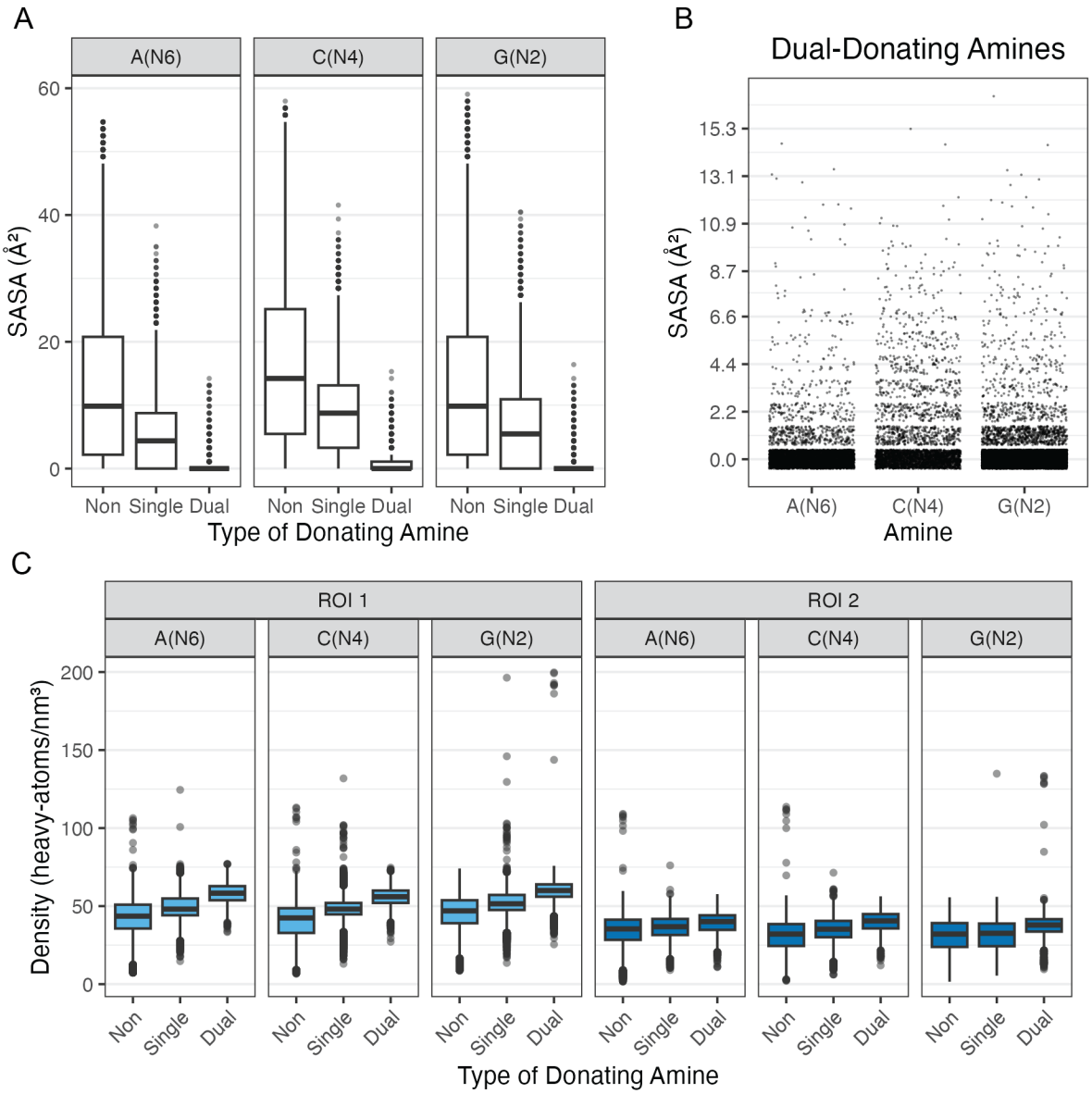

Figure S3. Amine solvent accessibility distributions and surrounding density with outliers. (*A*) Solvent accessible surface area (SASA) values for the nitrogens of non-, single-, and dual-donating amines from each type of nucleobase. All adjusted p-values for SASA are less than 2.2×10^{-16} for the differences observed in the distributions within each of the three subplots (see Methods). These box plots correspond to the data presented in Figure 6A. (*B*) SASA values for the nitrogens of just the dual-donating amines from each type of nucleobase. Each point is jittered along the x- and y-axes and corresponds to the SASA value of the closest horizontal line. (*C*) Density of heavy atoms within the regions depicted in Figure 6B. All adjusted p-values for heavy atom density are less than 1×10^{-5} for the differences observed in the distributions within each of the six subplots. These plots are the same as Figure 6C except that outliers are included.

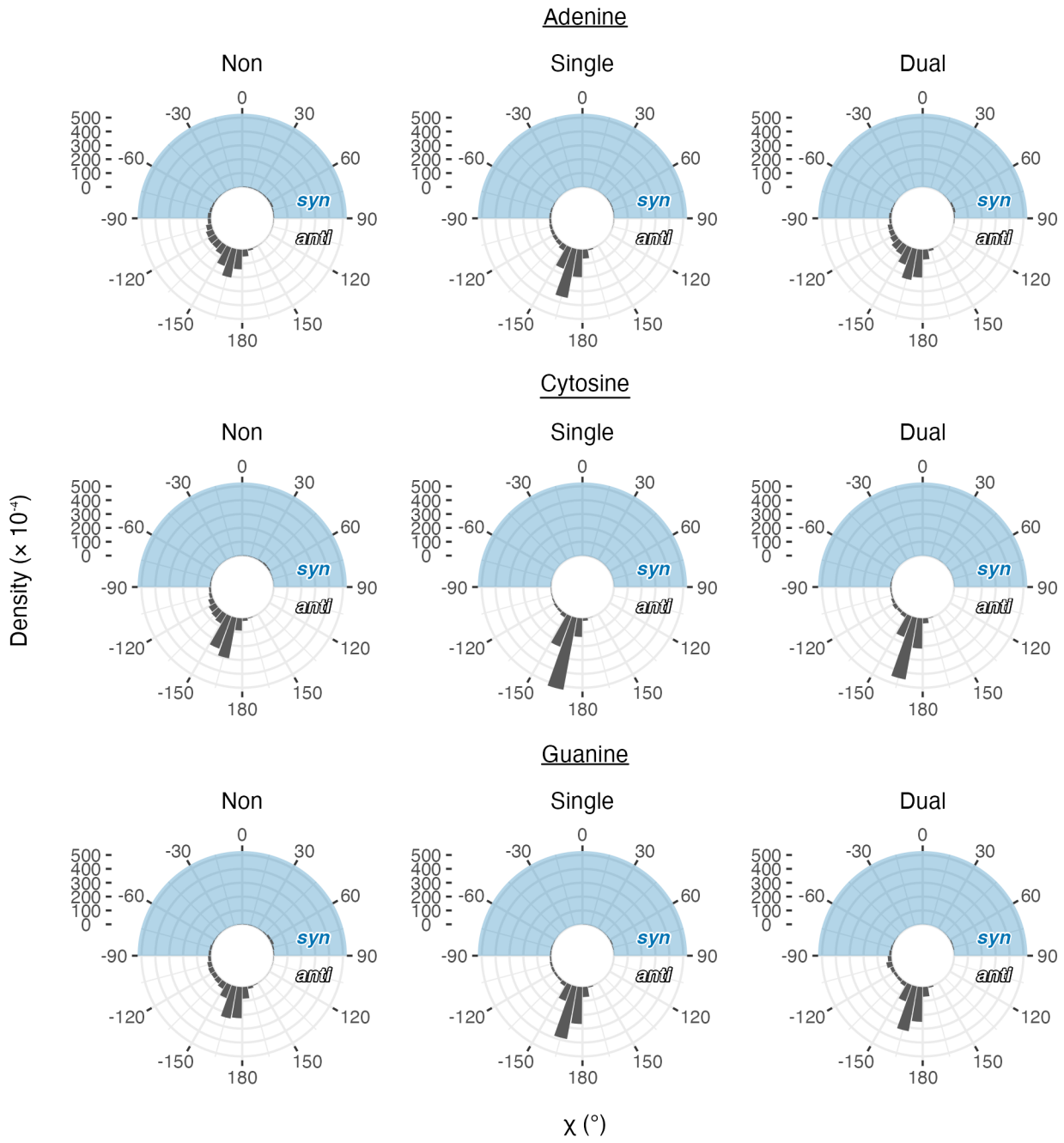

Figure S4. Radial density plots of *χ* dihedrals among residues that bear non-, single-, and dual-donating amines. The blue shaded region corresponds to nucleobases that adopt the *syn* conformation. All p-values are less than 1×10^{-3} for the differences observed in the distributions within each of the A, C, and G series of plots (see Methods). Another version of these plots is depicted in Figure 7B which focuses on the densities of the minor population.

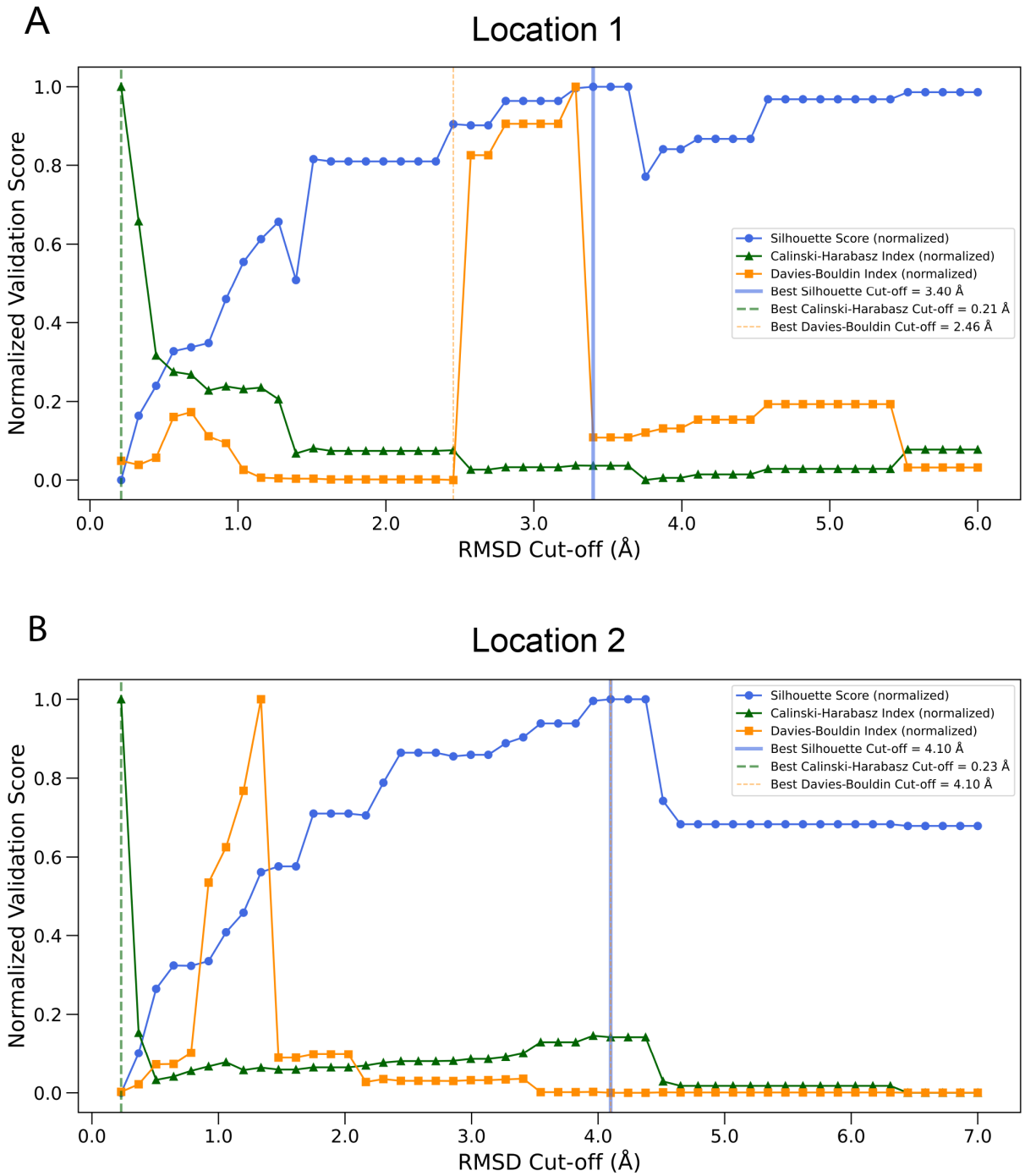

Figure S5. Three validation metrics calculated across 50 RMSD cut-off values. Values for (*A*) Location 1 fragments range from 0.21 Å to 6.0 Å, and (*B*) Location 2 fragments range from 0.23 Å to 7.0 Å. The RMSD cut-offs selected to create the dendrograms depicted in Supplemental Figure S6 was based on the Silhouette scores.

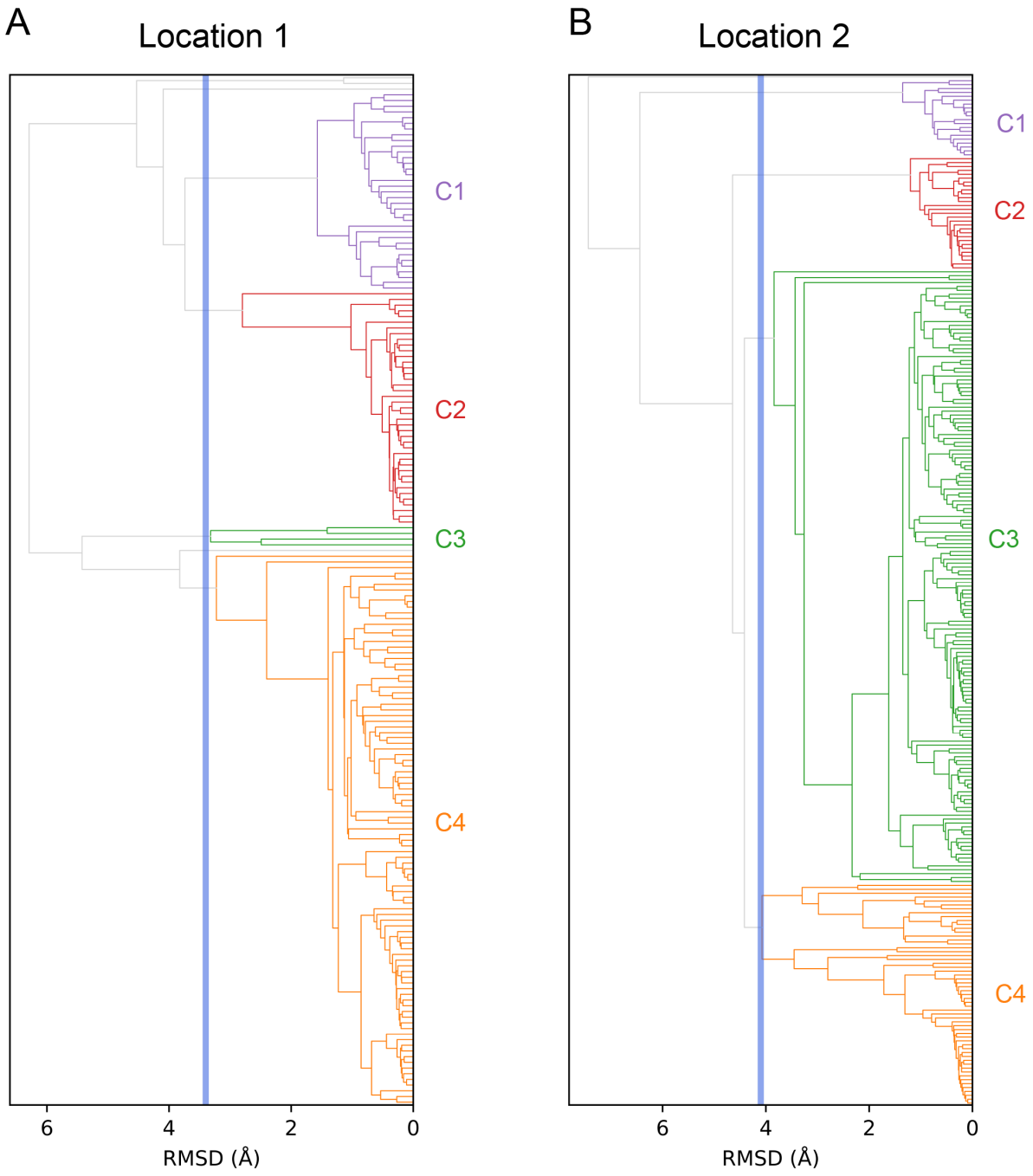

Figure S6. Dendrograms from hierarchical clustering. These include fragments from (*A*) Location 1 and (*B*) Location 2. Blue lines indicate the chosen RMSD cut-offs using the Silhouette scores (see Supplemental Figure S5). Location 1 contains 181 fragments and Location 2 contains 266 fragments.

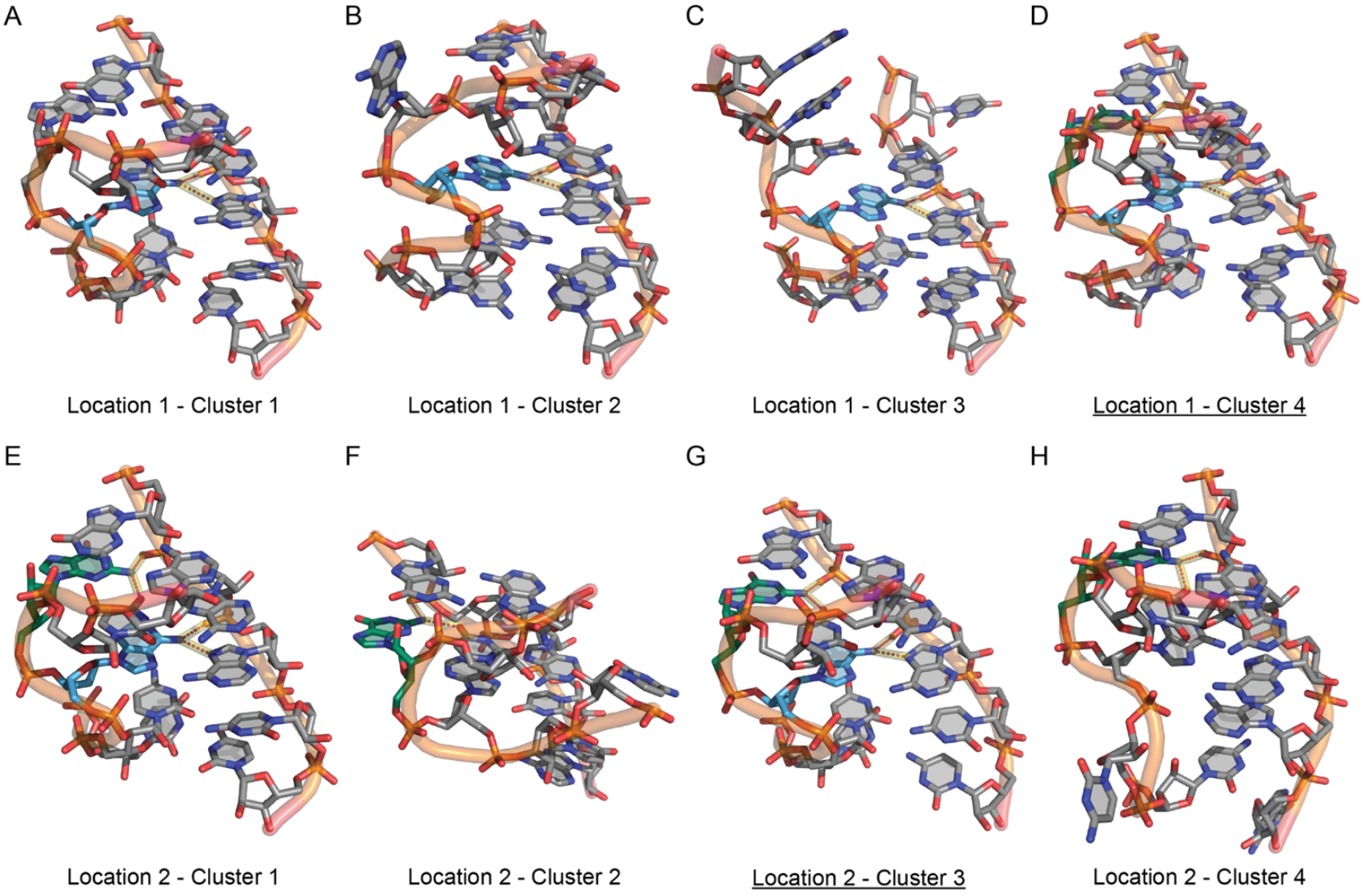
A
B
C
D
Location 1 - Cluster 1
Location 1 - Cluster 2
Location 1 - Cluster 3
Location 1 - Cluster 4
E
F
G
H
Location 2 - Cluster 1
Location 2 - Cluster 2
Location 2 - Cluster 3
Location 2 - Cluster 4

Figure S7. All representative structures from the cluster analyses. (*A*-*D*) Representative structures from the clusters of the Location 1 analysis with A's present in Location 1 colored blue. In (*D*), the G colored green and connected to the 3′-end of the blue A is present in Location 2. The structure in (*D*) is the same as that depicted in Figure 8E. In the four structures, the A's colored blue are A195 from chain BA of PDB ID 6TH6, A2023 from chain A5 of PDB ID 9CAI, A2396 from chain B5 of PDB ID 7O7Y, and A806 from chain S60 of PDB ID 6ZU5, respectfully (Sas-Chen et al. 2020; Sehgal et al. 2024; Bhatt et al. 2021; Ehrenbolger et al. 2020). (*E*-*H*) Representative structures from the clusters of the Location 2 analysis with G's present in Location 2 colored green. In (*E, G*), the A colored blue and connected to the 5′-end of the green G is present in Location 1. In the four structures, the G's colored green are G205 from chain 1A of PDB ID 9DFE, G1392 from chain iN of PDB ID 8RDV, G79 from chain 8 of PDB ID 8OVJ, and G458 from chain 1A of PDB ID 9DFE, respectfully (Jangra et al. 2025; Helena-Bueno et al. 2024; Rajan et al. 2024). Underlined labels indicate the associated structure belonging to the dominant cluster for that cluster analysis. In all panels, magenta dots highlighted in yellow depict H-bonds from dual-donating amines.

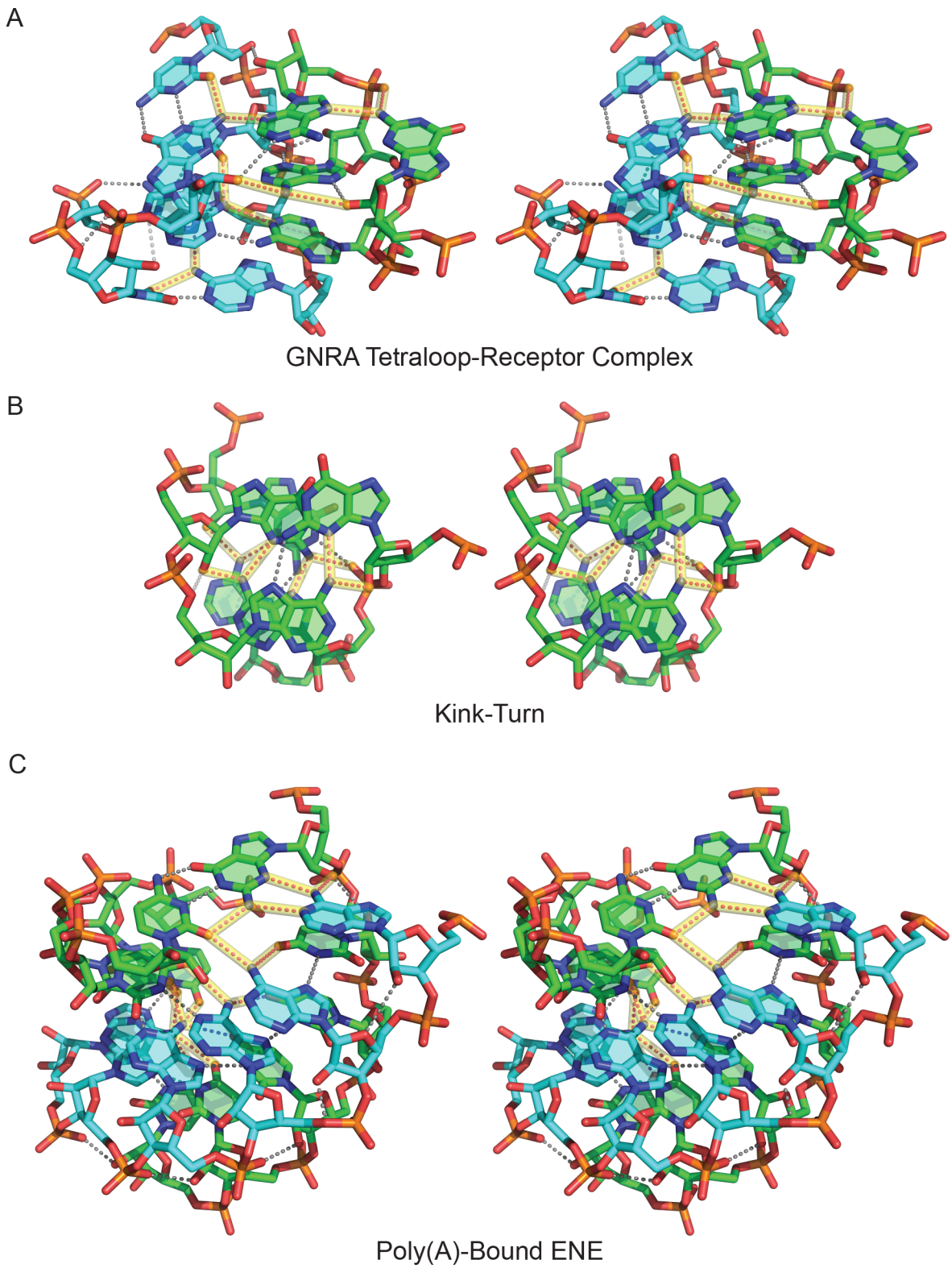

Figure S8. Cross-eye stereoviews of structured RNAs enriched in dual-donating amines. Depicted are the (*A*) GNRA tetraloop receptor bound to a GAAA tetraloop, (*B*) kink-turn, and (*C*) poly(A) strand bound to an ENE from Figure 9.

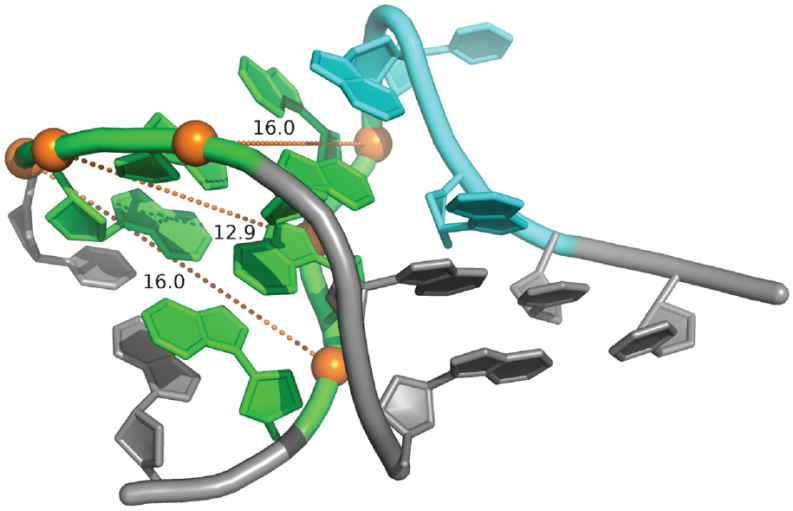

Figure S9. The sheared GA base pairs in the kink-turn hold the phosphate backbone closer together. Depicted is the kink-turn with interstrand phosphate distances of 16.0, 12.9, and 16.0 Å for each pair of phosphates (orange) on the 5′-end of each of the three sheared GA base pairs.

Supplemental References

Bhatt PR, Scaiola A, Loughran G, Leibundgut M, Kratzel A, Meurs R, Dreos R, O'Connor KM, McMillan A, Bode JW, et al. 2021. Structural basis of ribosomal frameshifting during translation of the SARS-CoV-2 RNA genome. *Science* **372**: 1306–1313. doi: 10.1126/science.abf3546

Ehrenbolger K, Jespersen N, Sharma H, Sokolova YY, Tokarev YS, Vossbrinck CR, Barandun J. 2020. Differences in structure and hibernation mechanism highlight diversification of the microsporidian ribosome. PLoS Biol 18: e3000958. doi: 10.1371/journal.pbio.3000958

Helena-Bueno K, Rybak MYu, Ekemezie CL, Sullivan R, Brown CR, Dingwall C, Baslé A, Schneider C, Connolly JPR, Blaza JN, et al. 2024. A new family of bacterial ribosome hibernation factors. *Nature* **626**: 1125–1132. doi: 10.1038/s41586-024-07041-8

Rajan KS, Aryal S, Hiregange D-G, Bashan A, Madmoni H, Olami M, Doniger T, Cohen-Chalamish S, Pescher P, Taoka M, et al. 2024. Structural and mechanistic insights into the function of Leishmania ribosome lacking a single pseudouridine modification. *Cell Rep* **43**: 114203. doi: 10.1016/j.celrep.2024.114203

Sas-Chen A, Thomas JM, Matzov D, Taoka M, Nance KD, Nir R, Bryson KM, Shachar R, Liman GLS, Burkhart BW, et al. 2020. Dynamic RNA acetylation revealed by quantitative cross-evolutionary mapping. *Nature* **583**: 638–643. doi: 10.1038/s41586-020-2418-2

Sehgal E, Wohlenberg C, Soukup EM, Viscardi MJ, Serrão VHB, Arribere JA. 2024. High-resolution reconstruction of a *C. elegans* ribosome sheds light on evolutionary dynamics and tissue specificity. *RNA* **30**: 1513–1528. doi: 10.1261/rna.080103.124

Wang Y, Guan Z, Wang C, Nie Y, Chen Y, Qian Z, Cui Y, Xu H, Wang Q, Zhao F, et al. 2022. Cryo-EM structures of *Escherichia coli* Ec86 retron complexes reveal architecture and defence mechanism. *Nat Microbiol* **7**: 1480–1489. doi: 10.1038/s41564-022-01197-7

Jangra M, Travin DY, Aleksandrova E V., Kaur M, Darwish L, Koteva K, Klepacki D, Wang W, Tiffany M, Sokaribo A, et al. 2025. A broad-spectrum lasso peptide antibiotic targeting the bacterial ribosome. *Nature* **640**: 1022–1030. doi: 10.1038/s41586-025-08723-7